

<https://doi.org/10.1038/s42003-025-08748-8>

A single-cell atlas of mouse central nervous system immune cells reveals unique infection-stage immune signatures during the progression of meningitis caused by *Streptococcus suis*



Xuan Jiang^{1,4}, Jikun Mei^{1,4}, Junhui Zhu¹, Yanyan Tian¹, Tong Wu¹, Ziheng Li¹, Zengshuai Wu¹, Tamim Abdelaal^{2,3}, Fengyang Li¹, Na Li¹ & Liancheng Lei¹

Meningitis caused by *Streptococcus suis* serotype 2 (SS2) in humans and pigs is an acute nervous disorder associated with serious sequelae. Bacterial meningitis is tightly associated with immune cell responses and the local immune microenvironment. However, the dynamic changes of the immune system during the disease progression in the brain remains unclear. Here, single-cell mass cytometry analyses are used to comprehensively profile the composition and phenotypes of female mouse brain immune cells at different stages of SS2 meningitis. Ten major immune cell lineages are identified among which T cells and dendritic cells significantly increased during meningitis, with B cells increasing in the late stage. Specifically, SS2⁺PD-L1⁺ neutrophils with strong phagocytosis, bactericidal and apoptotic effects accumulate in the acute phase of SS2 infection. Microglia sequentially display the features of homeostasis, proliferation, and activation (enhanced MHCII and TLR2 signals and TNF- α secretion) during the process of meningitis. Both border-associated and monocyte-derived macrophages contribute to the process of SS2-induced meningitis, exhibiting upregulation of CD38 and MHCII. Interestingly, CD11c⁺CD8⁺T cells are the main contributor of IFN- γ and specifically appeared during SS2 infection. In addition, the appearance of other lymphocytes such as CCR6^{+/lo} B cells, CX3CR1⁺ NK and MHCII⁺ ILC3 are related to the progression of meningitis. Moreover, correlation analysis between the composition of immune cell clusters and the SS2 infection process yield a dynamic immune landscape in which key immune clusters, including some previously unidentified, mark different stages of infection. Together, these data reveal the unique infection-stage immune microenvironment during the progression of meningitis caused by SS2 and provide resources for the analysis of immunological pathogenesis, potential diagnostic markers and therapeutic targets for bacterial meningitis.

The existence of significant communication between the immune system and the central nervous system (CNS) is generally accepted. As an important component of the CNS, the brain includes parenchyma, the meningeal layer, and ventricles containing the choroid plexus and cerebrospinal fluid, as well as the blood-brain barrier (BBB), the blood-leptomeningeal barrier (BLMB) and the blood-CSF barrier (BCSFB)¹. The BBB and BLMB directly separate

the circulating blood from CNS surroundings. The BCSFB exists out of an epithelial layer interconnected by tight junctions, preventing cells from the accessible choroid plexus stroma to enter the CSF². However, this barrier can be disrupted during inflammation³. Immune cell migration across the BBB comprises a conserved cascade of sequential steps. Immune cells can enter the perivascular and leptomeningeal spaces to a limited degree. The dura

A full list of affiliations appears at the end of the paper. e-mail: vetlina2013@126.com; leiliancheng@163.com

mater and choroid plexus have a fenestrated vasculature and are therefore more accessible. Microglia are resident immune cells in the CNS, which contribute to neuronal synapse shaping and immune surveillance under homeostatic and disease conditions^{4,5}. Outside the parenchyma, the blood-accessible border regions of the brain contain a diverse immune repertoire. Immune surveillance is mediated by dendritic cells (DCs) and CNS border-associated macrophages (BAMs) that line the meninges, choroid plexus, and perivascular spaces^{6,7}. Recent studies have also shown that the meninges have a lymphohematopoietic microenvironment that exists at the border of the CNS, and early B cell subsets that normally exist in the bone marrow can also be found in the dura mater under steady-state conditions⁸. In summary, numerous cells with dynamic, complex and diverse characteristics, and their interactions with other immune subpopulations, together shape the immune microenvironment of the CNS.

Streptococcus suis type 2 (SS2) is a re-emerging zoonotic pathogen that causes severe disease, mainly meningitis, in pigs and people who have occupational contact with pigs or pork^{9,10}. If SS2 fails to cause death via septic shock, bacteria in the blood can cross the BBB or BSCFB and enter the CNS to induce meningitis¹¹. It has been reported that several SS2 components can mediate the release of pro-inflammatory cytokines¹² and contribute to the development of meningitis, including capsular polysaccharide (CPS), hemolysin, and muramidase-releasing protein (MRP)^{13,14}. *Streptococcus pneumoniae* activated nociceptors through its pore-forming toxin pneumolysin, hijacking CGRP-RAMP1 signaling in meningeal macrophages to facilitate brain invasion¹⁵. Overproduction of proinflammatory cytokines is considered the most important cause of SS2 meningitis as well as toxic shock-like syndrome (STSLs)^{16,17}. Therefore, the immune cell response in the brain may be closely related to the progression of meningitis through releasing complex cytokines. Pathogens may induce overproduction of pro-inflammatory cytokines, leading to septic shock or the recruitment and activation of leukocyte populations, leading to acute inflammation of the CNS. Dominguez-Punaro et al. demonstrated for the first time that SS2 invades the CNS and causes activation of microglia and astrocytes, and the cytokines it secretes may induce Th1-type immune responses^{16,18}. During neuroinflammation, the composition of immune cells in the CNS changes dramatically. During the pathogenesis of meningitis, *S. suis* interacts with a diverse array of immune cells, such as neutrophils, monocytes, lymphocytes, DCs, and microglia, and uses a series of virulence factors to evade the host's innate and adaptive immune defenses^{19,20}. The specific immune cell types involved in the process of neuroinflammation caused by bacterial meningitis and their unique functions have not yet been explored. The high-dimensional composition and marker characteristics of heterogeneous CNS-infiltrating immune cells may identify new biological markers and develop novel therapeutics.

High-dimensional mass cytometry can detect over 40 marker expression on the cells in the brain parenchyma simultaneously at a single-cell resolution²¹. Here, we used mass cytometry to identify immune cell subpopulations involved in the progression of meningitis post-SS2 infection. We further defined the immune response phenotypes and characteristics of lymphoid and myeloid cells (including T cells, B cells, innate lymphoid cells (ILCs), DCs, monocytes, macrophages and microglia) during meningitis. This study extensively describes the relative abundance of brain immune cell infiltrating populations in the process of Gram-positive bacterial meningitis as exemplified by SS2 infection and comprehensively maps the brain tissue immune cell landscape in response to meningitis.

Results

SS2-infection shapes the major immune lineages in mouse brain

To capture the complexity of cellular phenotypes and cell numbers in brain tissue during the pathogenesis of meningitis in mice infected with SS2 (Fig. 1A), we first developed a mouse meningitis model²². The mice showed characteristics of sepsis 24 h post-infection with SS2 as the mortality was the highest. Mice infected with SS2 for 5 days displayed typical meningitis characteristics (neurological symptoms) with frequent head tremors, uncontrolled nodding, turning, and spontaneous turnover. The bacterial

load in the brain reaches peak at SS2-24h, and as neurological symptoms appear, the bacterial load gradually decreases over time²². Next, we developed a mass cytometric panel consisting of 42-metal labeled antibodies (Supplementary Table 1), which includes lineage markers representing cell differentiation, activation, adhesion, and anti-SS2 polyclonal antibodies. This panel enabled the analysis of immune cells in the brain of mice without and with SS2 infection. Single, live CD45^{+/lo} immune cells were distinguished by DNA, CD45 antibody staining, and physical parameters (event length, residual, width, center) (Supplementary Fig. 1A). All antibodies showed a clear discrimination between antibody-positive and -negative cells (Supplementary Fig. 1B). To determine immune lineage heterogeneity, 4 × 10⁶ immune cells derived from 20 brain samples were first selected at the overall level and embedded into the second level of H-SNE analysis in Cytosplore^{23,24}. Next, we determined 10 major immune lineages based on the marker expression profiles and cell density features (Fig. 1B and C), among which the myeloid lineage included microglia (CD45^{lo}CD11b⁺CX3CR1⁺), macrophage (CD45⁺CD3⁻CD19⁻NK1.1⁻Ly6G⁻F4/80⁺), neutrophils (CD45⁺CD3⁻CD19⁻NK1.1⁻Ly6G⁺), monocyte (CD45⁺CD3⁻CD19⁻NK1.1⁻Ly6G⁻Ly6C⁺/CD14⁺) and DCs (CD45⁺CD3⁻CD19⁻NK1.1⁻CD11c⁺MHCII⁺). Lymphoid lineages included CD4⁺T cells (CD45⁺CD3⁺CD4⁺), CD8⁺T cells (CD45⁺CD3⁺CD8⁺), $\gamma\delta$ T cells (CD45⁺CD3⁺TCR $\gamma\delta$ ⁺), B cells (CD45⁺CD19⁺) and ILCs (CD45⁺CD3⁻NK1.1⁻/IL-7Ra⁺) (Fig. 1D). Quantification of the counts of the major lineages at each time point revealed that during sepsis (24 h after SS2 infection), neutrophils and monocytes exhibited strong infection time specificity, i.e., their proportion increased significantly, especially SS2⁺ neutrophils (Fig. 1E-F). The number of CD4⁺T, CD8⁺T, $\gamma\delta$ T, ILCs, microglia, DCs, and macrophages during meningitis (5 d to 15 d after SS2 infection) was significantly higher than that in control and mice infected for 24 h (Fig. 1F). During the period of neurological symptoms, the B cell numbers also continued to increase. Conversely, the proportion of microglia significantly decreased throughout the entire disease stage (Supplementary Fig. 2). Together, our data indicate that SS2 infection shapes the major immune lineages in the mouse brain as meningitis develops.

Microglia sequentially display features of homeostasis, proliferation, and activation during the process of meningitis

Microglia, as innate immune cells of the CNS, play a key role in brain development, immune defense and maintenance of CNS homeostasis²⁵. First, a t-SNE dimensional reduction analysis was performed on the collected microglia population (1,519,032 cells). Based on the density features of the t-SNE-embedded cells and using Gaussian mean-shift clustering analysis, four phenotypically distinct clusters were identified (Fig. 2A-C). Microglia subsets displayed strong specificity as meningitis progressed (Fig. 2D). These clusters were further divided into two main meta-clusters by unbiased hierarchical clustering of the heat map based on the differential expression of markers such as TLR2, MHCII, Ki-67, and F4/80 (Fig. 2E, Supplementary Fig. 3A). During the time course of infection, the stacked bar analysis identified dramatic changes in immune cell composition (Fig. 2F). Microglia in the homeostatic environment of control brains are characterized by high expression of the core gene *P2ry12*²⁶⁻²⁸, which inhibits the development of neuroinflammation²⁹. The expression of *P2RY12* in the microglia of the control group was significantly higher than those of all SS2-infection groups. When neurological symptoms occurred, the level of *P2RY12* was further reduced compared with SS2 infection at 24 h (Fig. 2G). At 24 h of SS2 infection, the number of Ki-67 positive microglia increased significantly, and these Ki-67⁺ microglia did not express activated markers such as MHCII and TLR2 (Fig. 2G, Supplementary Fig. 3B, C). The results are consistent with a previous study in which Ki-67⁺ microglia generally appear after nerve injury³⁰. Microglia lost their ramified morphology and assumed a more amoeboid morphology, characteristic of activated microglia. Microgliosis, a hallmark of neuroinflammation and infection³¹, was also observed after SS2 infection as shown by the increase in Ki-67⁺ microglia (Fig. 2H). The main phenotype of microglia with neurological symptoms was MHCII⁺F4/80⁺TLR2⁺Ki-67⁺ (Cluster 1) (Supplementary Fig. 3D).

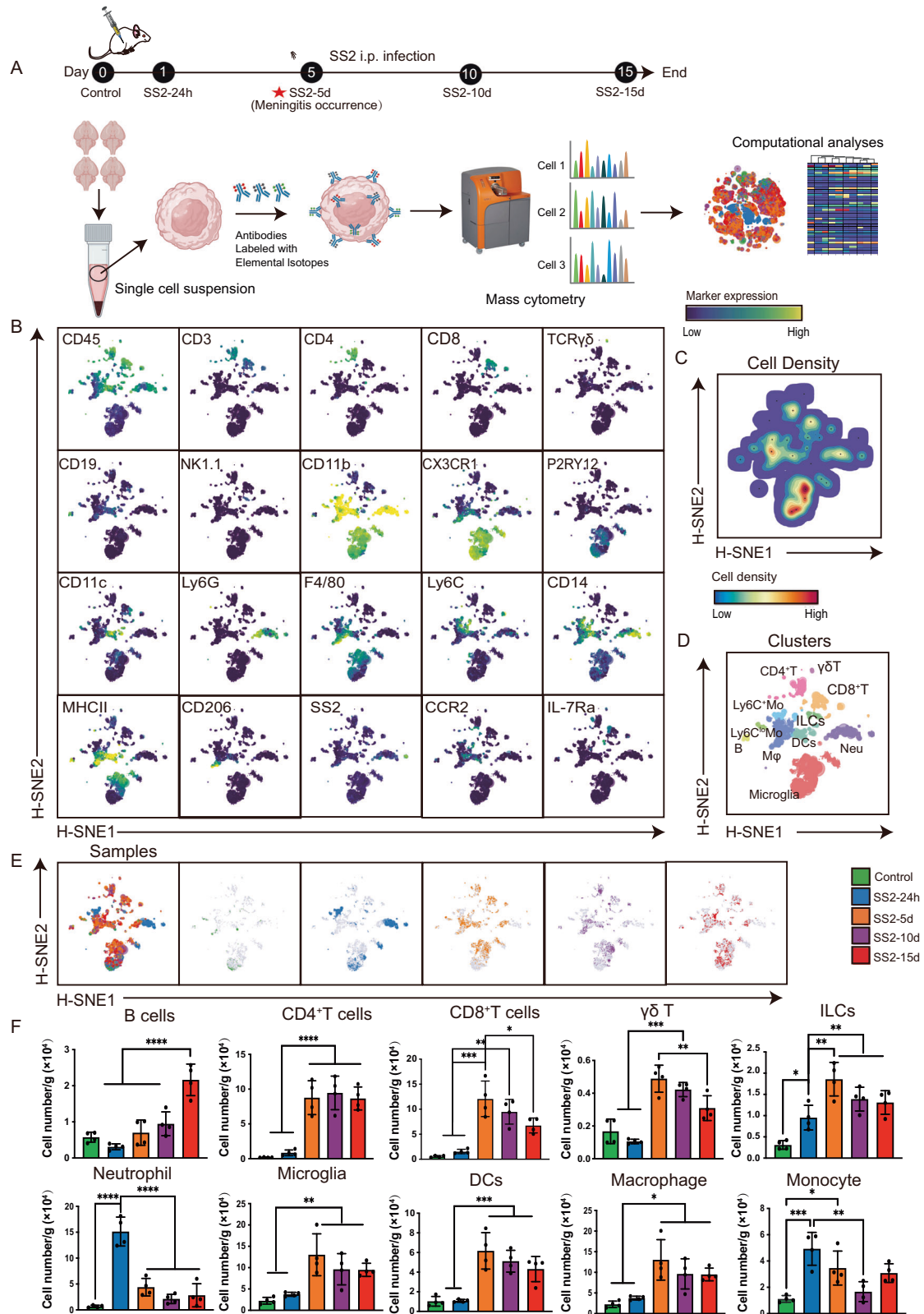
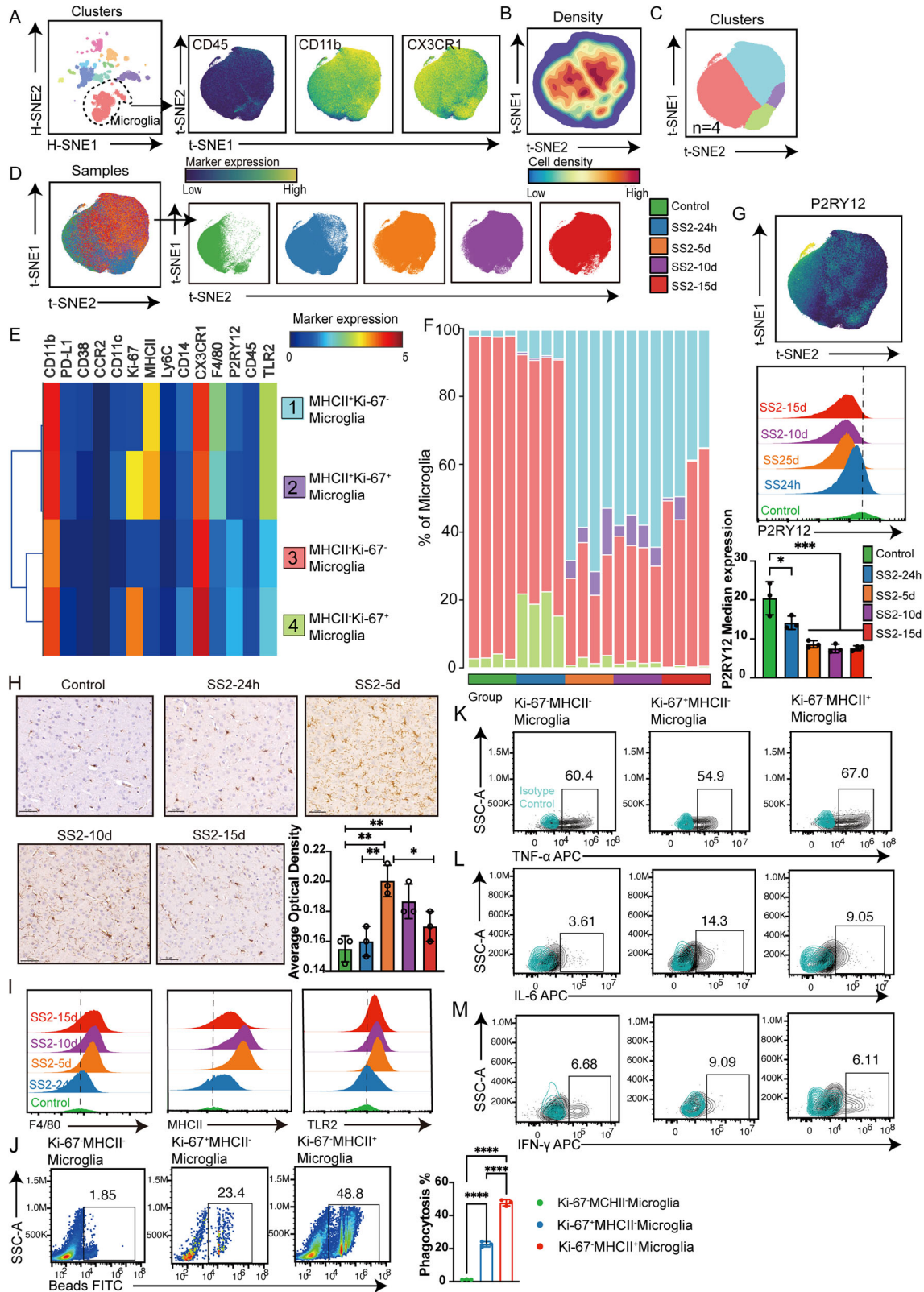


Fig. 1 | CyTOF identifies Brain-associated leukocyte diversity in mice after SS2 infection. **A** Schematic representation of the experimental design. **B** H-SNE embeddings of 4.8×10^6 immune cells derived from the female mouse brain ($N = 20$, each sample contains brains of six mice) at the overview level. Each dot represents a landmark, whose size is proportional to the number of cells it represents. Colors indicate the ArcSinh5-transformed expression value of each indicated marker. **C** H-SNE plots show cell densities. **D** H-SNE plots show the major immune lineage

cluster partitions in different colors. **E** H-SNE map displaying all immune cells in each group from the brain of healthy and SS2-infected ICR mice analyzed by CyTOF. **F** Cell counts of each major immune lineage during SS2 infection. $N = 4$ in each group. Error bars represent the median \pm SEM. A one-way ANOVA or Dunnett's test was performed for analysis of multiple groups. P value < 0.05 (*); $p < 0.01$ (**); $p < 0.001$ (***) ; NS no significant difference.



There was no significant difference in the expression of F4/80 and TLR2 during neurological symptom progression, while MHC-II expression decreased significantly in the late stage of meningitis (Fig. 2I, Supplementary Fig. 3E).

Next, we detected the phagocytic function of the three dominant phenotypes of microglia at different stages of SS2-infection. Ki-67 MHCII⁺

microglia had the strongest phagocytic ability, followed by Ki-67⁺MHCII⁻ and Ki-67 MHCII⁺ microglia (Fig. 2J). Interestingly, Ki-67 MHCII⁺ microglia had a strong ability to secrete TNF-α (Fig. 2K), while Ki-67⁺MHCII⁻ microglia is the main contributor of IL-6 and IFN-γ during acute infection (Fig. 2L-M). Therefore, microgliosis, morphological changes and inflammatory cytokine expression, indicate robust neuroinflammation

Fig. 2 | Heterogeneous composition and phenotypic changes of microglia after SS2 infection. A–C t-SNE map, density map and boundaries of clusters of microglia are shown. t-SNE plot shows expression of the indicated marker. The density plot shows the local density of cells and the cluster partition shows the boundaries of the four clusters of microglia. D t-SNE plots of microglia from the CNS samples of five groups are shown. E A heatmap displays the median marker expression value and hierarchical clustering of the markers for nine clusters identified in C. F Vertical bar graph depicting the composition of the microglia compartment in each mouse brain sample at the indicated time points. The colored segment lengths represent the proportion of cells as a percentage of total microglia in each sample. Colors as in E. G Median expression and statistical result of P2RY12 expression on microglia of control and SS2 infected mice ($N = 3$) at different stages. H Immunohistochemical

images of IBA-1⁺ microglia in control and SS2-infected mice ($N = 3$) at different stages. Scale bar = 50 μm . I Median expression of F4/80, MHCII and TLR2 expression on microglia in healthy and infected SS2 mice at different stages. J The phagocytic ability of three phenotypes microglia (Ki-67⁺ MHCII⁺ microglia, Ki-67⁺ MHCII⁺ microglia and Ki-67⁺ MHCII⁺ microglia) at different stages of SS2 infection was detected by flow cytometry. Four female mouse brains were pooled in one sample, $N = 3$. K–M The levels of cytokines (TNF- α , IL-6 and IFN- γ) secreted by three types of microglia were detected by flow cytometry. Error bars represent the median \pm SEM. A one-way ANOVA or Dunnett's test was performed for analysis of multiple groups. Student's t-test was used to compare the two groups. P value < 0.05 (*); $p < 0.01$ (**); $p < 0.001$ (***) ; NS no significant difference.

and tissue damage. Taken together, these results indicate that SS2 infection leads to microglia proliferation, followed by microglia activation during the meningitis disease course.

Both monocyte-derived and border-associated macrophages contribute to the process of SS2-induced meningitis

CNS macrophages include microglia and border-associated macrophages (BAMs). Additionally, during infection peripheral myeloid cells can enter the borders and parenchyma, leading to inflammation^{23,22,33}. Therefore, we focused on these cells to study their response to SS2 as they were shown in other infection models to impact the infection course. Based on the density features of the t-SNE-embedded cells, we identified 10 phenotypically distinct clusters (Fig. 3A, B). The phenotypic heatmap and proportional bar chart identified the main population of macrophages in the control mouse brain under physiological conditions as CD38⁺CD206⁺MHCII⁺ BAMs (Cluster 6) (Fig. 3D, E). Twenty-four h post-SS2 infection (the acute phase of infection), monocyte-derived macrophages (Clusters 5) with low expression of CD14 and no expression of MHCII invaded the brain in notably higher proportions compared to those observed in the control and neurological symptom groups (Fig. 3C, D). In addition, monocyte-derived macrophages expressed higher adhesion-related markers, i.e., CD45, CD44 and CD49d (Fig. 3C), showing that CD44 and CD49d can be used to distinguish between resident and infiltrated cells³⁴. Similar to the microglia, monocyte-derived macrophages and BAMs with an increased proportion during neurological symptoms also upregulated activation markers such as MHCII (Fig. 3C, D). BAMs could be reliably distinguished from monocyte-derived macrophages using the expression of relevant markers F4/80, Ly6C, CD38, MHCII and CCR2³⁴ (Fig. 3C, D). Nearly 90% of the macrophages in the brain of control mice were BAMs (cluster 6 and 8), further confirmed via immunofluorescence of the brain (Fig. 3F). The BAMs of control mice were evenly arranged in the pia mater area and perivascular space (Fig. 3F). Consistent with the mass cytometry results, immunofluorescence staining identified that CD38 expression increased with the progression of infection (Fig. 3F, Supplementary Fig. 4A). Within the choroid plexus, BAMs proliferated during neurological symptoms neurological symptoms, which was less apparent within the leptomeninges and then this nicely defines the resident macrophage response (Fig. 3G, Supplementary Fig. 4B). Monocytes appeared at the stage of neurological symptoms (Supplementary Fig. 4C–E). Meanwhile, the adoptive transfer of monocytes confirmed that macrophages in the brain could be derived from monocytes (Supplementary Fig. 4F). In conclusion, based on phenotypic differences, resident macrophages in the brain during meningitis can be distinguished from infiltrating monocyte-derived macrophages, and both BAMs and monocyte-derived macrophages have phenotypic characteristics related to infection.

Neutrophils accumulate in the brain in the acute but not meningitic stage of SS2-infection

The substantial inflammation characteristic of bacterial meningitis leads to further recruitment of neutrophils and inflammatory cells³⁵. Under physiological conditions, a small number of neutrophils were present in the

brain, with a peak at 24 h after SS2 infection, while the number decreased sharply after the onset of neurological symptoms compared with the acute infection period (Supplementary Fig. 5A–B). Nine clusters were identified in all neutrophils (480,000 cells), which displayed different disease signatures as meningitis proceeded (Fig. 4A–E). The phenotype of neutrophils under physiological conditions was mainly non-activated, with a phenotype of CD44⁺CD14^{lo}TLR2^{lo} (Clusters 3) (Fig. 4D, E, Supplementary Fig. 5D). After 24 h of SS2 infection, we observed a large number of Ly6G⁺ neutrophils around the pia mater and choroid plexus (Supplementary Fig. 5B, C). PD-L1 is upregulated in neutrophils and correlates with sepsis-induced immunosuppression³⁶. Interestingly, SS2⁺PD-L1⁺ neutrophils were specific to SS2 infection for 24 h (the acute infection period) (Fig. 4F, Supplementary Fig. 5E). Compared with PD-L1⁺ neutrophils, PD-L1⁺ neutrophils exhibited significantly higher rates of apoptosis (Fig. 4G). In addition, the phagocytic capacity of PD-L1⁺ neutrophils were stronger than that of PD-L1⁺ neutrophils (Fig. 4H). Confocal laser scanning also found that PD-L1⁺ neutrophils expressed higher levels of Histone H3 (H3) and myeloperoxidase (MPO) (Fig. 4I). These results suggested that PD-L1⁺ neutrophils are in a more activated stage post-SS2 infection. We also found that the neutrophils that appeared 24 h following SS2 infection had the common characteristics of high expression of CD14 and TLR2 (Fig. 4J). The expression of CD14 peaked at the acute stage of infection with low or no expression in the brain of normal mice, and medium expression in mice with neurological symptoms (Fig. 4J), suggesting that CD14 expression on the surface of neutrophils can be used as an indicator for different stages of meningitis. We also found that the percentage of two CX3CR1⁺ neutrophil clusters (Clusters 5 and 6) increased significantly at 24 h after SS2 infection and at the stage of neurological symptoms, among which Cluster 5 also expressed MHCII (Fig. 4D–E, Supplementary Fig. 5F). These findings suggested that neutrophils passed from the peripheral circulation (via chemotaxis) to the brain and then acquired the meningitis-specific phenotype. Moreover, cluster 8 (CD38⁺CD8^{lo}) specifically increased in the stages of infection involving neurological symptoms. Interestingly, cluster 8 expressed low CD8 (Supplementary Fig. 5G–H). Hence, our data revealed substantial neutrophil heterogeneity and identified cell subpopulations specific to each stage of SS2-induced meningitis.

Phenotypic alterations of T and B cells during meningitis development

Compared with control mice, we found that T cells were the largest group invading brain tissue during the development of meningitis (Fig. 1F), suggesting the important role of T cells in the process of SS2-induced meningitis. Consistent with mass cytometry data, we observed a large number of T cells in the leptomeninges and choroid plexus after 5 days of SS2 infection (Fig. 5A). To explore disease-specific changes in T cells with the development of SS2 meningitis, we divided CD3⁺T cells into 13 different cell clusters, including 5 CD4⁺T (T1–T4, T12), 6 CD8⁺T (T5–T9, T13), 2 $\gamma\delta$ T (T10–T11) (Fig. 5B–D). Next, we compared the distribution of each T cell subset among each group and found, compared with the control group, that the proportion of CCR2⁺Tregs increased throughout the entire SS2 infection stage (Fig. 5D–F). MHCII⁺CD4⁺T cells can induce more extensive

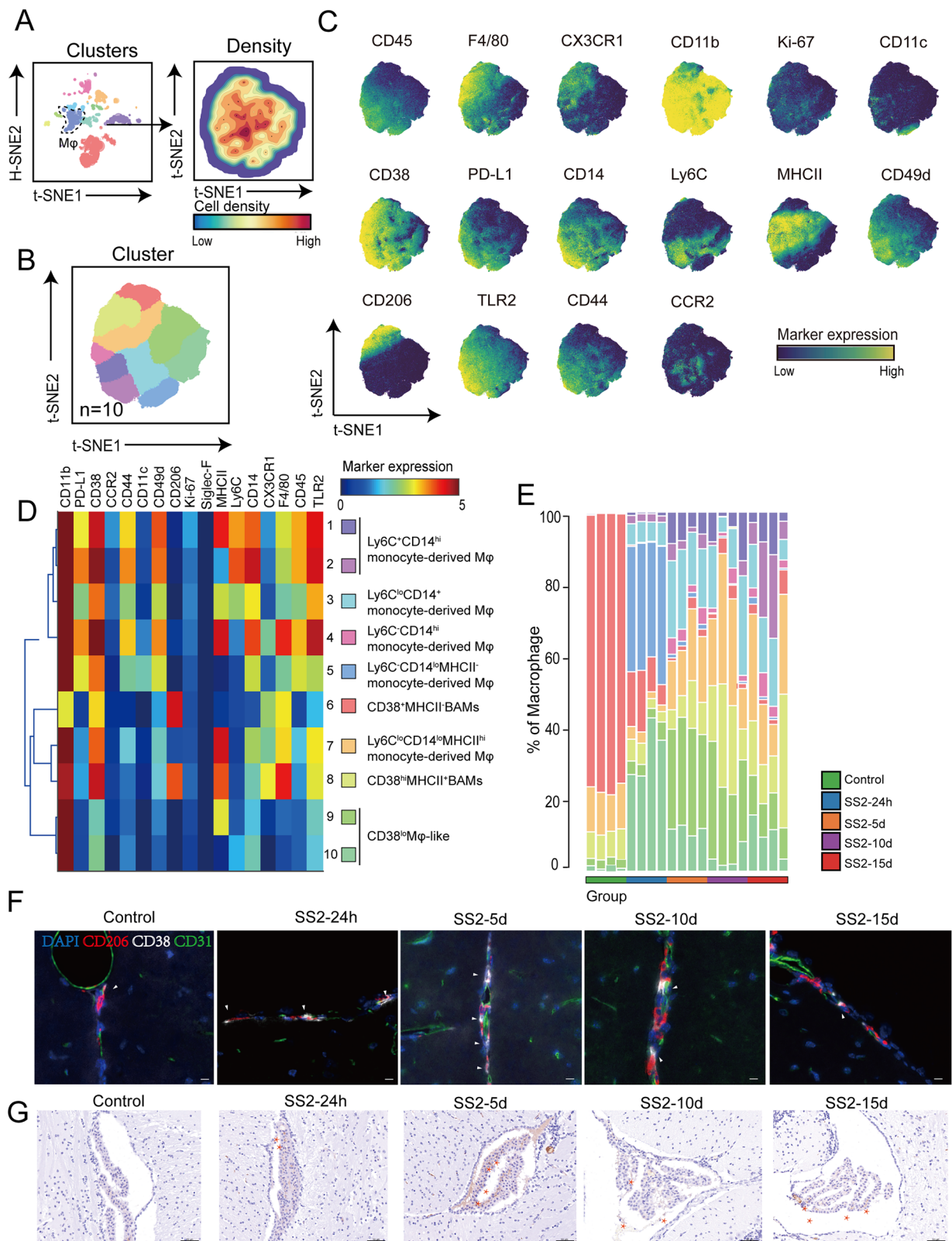
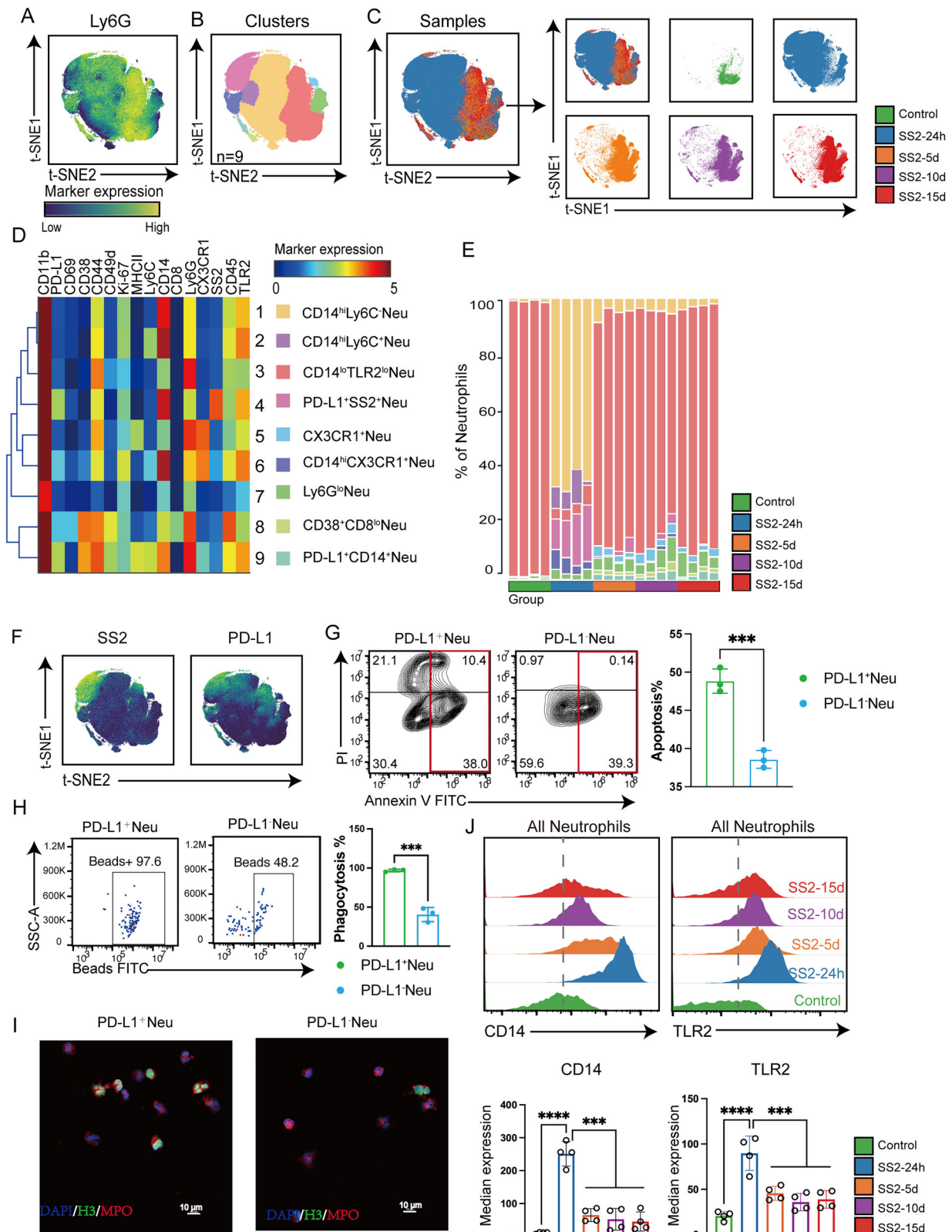


Fig. 3 | BAMS and peripheral invasive macrophages show distinct phenotypes in the brain. **A**, **B** The density map and the boundaries of clusters of macrophages are shown. The density map shows the local density of cells and the cluster partitioning shows the boundaries of 10 clusters of macrophages. **C** t-SNE maps showing the expression of specific marker molecules in macrophages. **D**, **E** Phenotypic heatmap and bar stacking charts show the phenotypic characteristics of the 10 identified

macrophage clusters and their distribution in each sample. **F** Control and SS2 infected mouse brains and coronal sections at the pia mater area and perivascular space, stained for indicated markers. CD206 (red), CD38 (white), and blood vessels were marked in green. Scale bar = 20 μ m. **G** Choroid plexus immunohistochemical images of CD206⁺ BAMS in control and SS2-infected mice at different stages. Scale bar = 50 μ m.



inflammation and demyelinating lesions in mice with multiple sclerosis³⁷. Interestingly, CD11b^{hi}TLR2⁺MHCII⁺CD4⁺T cells (Cluster 12) accumulated significantly throughout the progression of meningitis (Fig. 5D, E, G). However, the percentage of CD11c⁺CD8⁺T (Clusters 8) significantly increased 24 h post-infection (Supplementary Fig. 6A). Next, we isolated CD11c⁺CD8⁺T cells and CD11c⁻CD8⁺T cells to examine their function, and

found that the CD11c⁺CD8⁺T cells mainly produced cytotoxin-related factors, such as Perforin and Granzyme B (Supplementary Fig. 6B) and IFN- γ (Supplementary Fig. 6C). Additionally, $\gamma\delta$ T cells occur mainly in healthy brain tissue (Fig. 5D, E). In summary, these results indicated that significant changes in T cell composition and functional molecule expression were identified in different stages of meningitis.

Fig. 4 | Heterogeneous cellular composition and phenotypic characteristics in neutrophils. **A** The t-SNE map of neutrophils shows the expression of Ly6G. **B** The t-SNE map shows the cluster partitions. **C** t-SNE plots of neutrophils derived from the brain samples of five groups are shown. Colors indicate different groups. **D, E** A heatmap displays the median marker expression value and hierarchical clustering of the markers for 9 clusters identified in **B**. Vertical bar graph depicting the composition of neutrophils in mice brain in indicated time points. The colored segment lengths represent the proportion of cells as a percentage of total neutrophils in each sample. Colors as in **D**. **F** t-SNE maps show the expression of PD-L1 and SS2 in neutrophils. **G** Apoptosis of PD-L1⁺ neutrophils and PD-L1⁻ neutrophils were

detected by flow cytometry. Four female mouse brains were pooled in one sample, $N = 3$. **H** The phagocytic capacity of PD-L1⁺ neutrophils and PD-L1⁻ neutrophils was detected by flow cytometry. Four female mouse brains were pooled in one sample, $N = 3$. **I** Laser confocal results showed the expression of H3 and MPO in PD-L1⁺ PMN and their negative counterpart. Scale bar = 10 μ m. **J** Median expression and statistical plots of CD14 and TLR2 expression on neutrophils in indicated groups. $N = 4$. Error bars represent the median \pm SEM. A one-way ANOVA or Dunnett's test was performed for analysis of multiple groups. Student's t-test was used to compare the two groups. P value < 0.05 (*); p < 0.01 (**); p < 0.001 (***) ; NS no significant difference.

We also observed a significant increase in the number of B cells in the pia mater and choroid plexus during the late stage of neurological symptoms (Supplementary Fig. 7A). We further divided B cells into seven clusters, among which resting state B cells (Cluster 7 CD45^{lo}CD19^{lo}MHCII⁻ B cells) constituted the majority of the B cell population in the brain of healthy mice (Supplementary Fig. 7A–C). It is worth noting that a CCR6⁺ B cells (Cluster 1 CCR6⁺MHCII^{hi}) were significantly increased only during meningitis (Supplementary Fig. 7D). In addition, there was a significant increase in CD11b⁺ B cell subsets (Clusters 3, 6) in mice with neurological symptoms, especially Cluster 6 (CD11b^{hi}CX3CR1⁺ B cells), whose proportion increased throughout the whole neurological symptom period, while the proportion of cluster 3 (CD11b^{lo} B cells) was significantly higher in the middle stages compared to the early and late stages of neurological symptoms (Supplementary Fig. 7E). The expression of functional markers on B cells, such as CD19, CCR6, CD38 and CD49d, also increased during the development of meningitis (Supplementary Fig. 7F). Thus, our data revealed specific B cell phenotypes in the development of meningitis, and that MHCII, CCR6, and CD11b expression of B cells can be used to mark different stages of meningitis.

CX3CR1⁺ NK and MHCII⁺ ILC3 accumulate in the meningitic mouse brain

Recent studies have shown that various subgroups of ILCs exist in the brain and have major roles in regulating BBB integrity, and brain homeostasis³⁸. Similar to the above analysis, we grouped ILCs and partitioned them into 13 cell clusters with distinct phenotypes, which mainly included NK and ILC3 (Lin⁻CD127⁺c-kit⁻) subsets (Fig. 6A, B). Distinct variations were evident in the composition of ILCs within the brains of healthy mice, as compared to those at different stages post-SS2 infection (Fig. 6B, C). In a healthy brain there were small amounts of NK and CD127⁺ILCs with the latter mainly composed of MHCII⁻ILC3 (Fig. 6B). Post-infection, there was an upregulation of CD11b and KLRG1 on NK cells (Fig. 6C, D). The proportion of CD11b^{lo/+}KLRG1⁺CX3CR1⁺ NK (Clusters 9–11) significantly increased 24 h post-SS2 infection (Fig. 6D, E), while CD11b⁺KLRG1⁺NK had significant increased CX3CR1 expression during neurological symptoms (Clusters 12–13) (Fig. 6D, E), suggesting that the increase in the proportion of CX3CR1⁺NK may be a signal for the occurrence of meningitis. In addition, three clusters of ILC3 (Clusters 1–3) were identified in mouse brain (Fig. 6B, F). During neurological symptoms, the proportion of inflammatory MHCII⁺ ILC3 (Clusters 3) was significantly increased (Fig. 6B, G). In summary, our results demonstrated the heterogeneity of ILC population in the mouse brain, in which CX3CR1⁺ NK and MHCII⁺ ILC3 accumulate in the brains of meningitic mice.

Immune-system-wide analysis identified correlations between immune cells during SS2 infection

To study the comprehensive immune spectrum after SS2 infection, a t-SNE analysis was performed on all brain tissue samples based on the cluster cell frequency of CD45^{+/lo} immune cells (Fig. 7A–C). This analysis identified a clear progression trajectory of different stages of SS2 infection, with samples from the acute infection period (SS2–24h) clearly distinguishable from those from the neurological symptom period, while samples from different periods of SS2-5d, SS2-10d, and SS2-15d, where neurological symptoms

appeared, were connected (Fig. 7A). Therefore, our findings indicated that there were cell progression patterns associated with development of meningitis during SS2 infection. To identify which cell clusters are closely associated with infection progression, a second t-SNE analysis was performed on the same data set to visualize the cellular network by clustering all clusters instead of samples (Fig. 7B). This approach identified the top six clusters contributing to infection time-specific t-SNE signatures (Table 1). The main types responsible for the immune cell signature in healthy brains were CD38⁺MHCII⁺BAMs, MHCII⁺Ki-67 Microglia, TLR2^{lo}CD11b⁺DCs and CD19^{lo}B. Twenty-four h post-SS2 infection, innate immune cells such CD14^{hi}TLR2⁺/CD14^{hi}CX3CR1⁺neutrophils, CD14^{lo}MHCII⁻ macrophages and Ly6C⁺CD14⁺/Ly6C⁺CD14⁺CX3CR1^{hi} monocyte dominated in the brain. After the onset of neurological symptoms, KLRG1⁺CX3CR1⁺CD8⁺Tem and CD11c⁺CD8⁺Tem were significantly enriched in the brain. In the middle stage of neurological symptoms (SS2-10d), the proportion of adaptive immune cells such as CD11b⁺CX3CR1⁺DCs, CD4⁺Tem and CD8⁺Tem cells increased. In the late stage of neurological symptoms (SS2-15d), the CCR6⁺MHCII^{hi} and CD11b^{+/lo} B cells clusters contributed the most (Table 1). Subsequent proportion correlation analysis of all clusters identified a strong infection time-specific pattern and further confirmed the top cluster identified in Fig. 7C. Proportion correlations were mainly between major subsets of lymphocytes (such as CD4⁺T, CD8⁺T, and ILC3) and DC and B cells (Table 1 and Fig. 7C). In the later stages of meningitis, B cells were the main contributor (Fig. 7C). Thus, the comprehensive analysis of immune responses during SS2 infection identified a highly dynamic landscape of time-dependent interconnected networks of innate and adaptive immune cell clusters.

Discussion

Bacterial meningitis is often accompanied by a strong immune response including the activation of inflammatory cells and their infiltration into the brain. Understanding the immune cell dynamic landscape during meningitis is crucial for identifying novel therapeutic approaches. There is still a lack of the composition and balance of the brain immune system in bacterial meningitis. In this study, we used CyTOF to construct a comprehensive unsupervised clustering and visualization map of different disease stages of SS2 induced meningitis at the single-cell protein level. This extensive analysis enabled the identification of previously unknown infiltrating immune populations in the brain after SS2 infection, demonstrating the phenotypic range and richness of resident myeloid cells and infiltrating cells.

Several studies have demonstrated that most infiltrating immune cells are mainly present at the borders of the brain (e.g., meninges and choroid plexus) rather than in the parenchyma^{2,6,7,32}, which are consistent with our results. The acute phase of SS2 infection (24 h post-infection) was characterized by a surge in neutrophils, particularly PD-L1⁺SS2⁺ subsets. The association of PD-L1⁺ neutrophils with sepsis-induced immunosuppression³⁹ aligns with their observed high apoptosis and phagocytic activity, suggesting a paradoxical role: while eliminating pathogens, these cells may simultaneously dampen excessive inflammation through PD-L1-mediated signaling. Our results with SS2 contrast with viral meningitis models, where neutrophil infiltration is minimal and delayed³³. Conversely, in parasitic meningitis caused by *Toxoplasma gondii*, neutrophils are rapidly recruited but exhibit IL-12-dependent anti-parasitic functions⁴⁰.

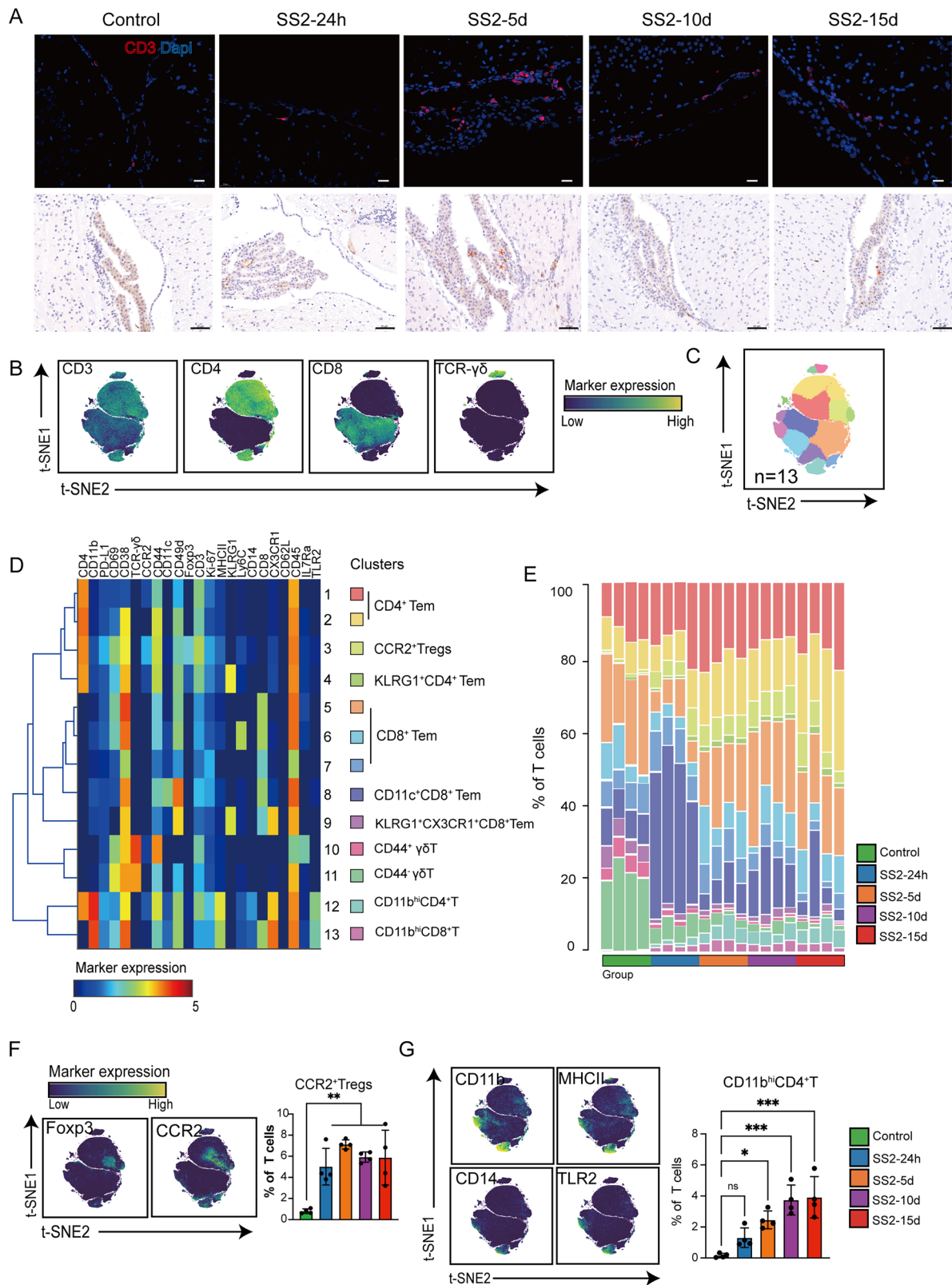


Fig. 5 | Characteristics of T cell phenotype changes during the progression of meningitis. **A** Control and SS2 infected mouse brains and coronal sections at the leptomeninges and choroid plexus, stained for anti-CD3. Scale bar = 20 μ m. Immunohistochemical images of CD3⁺ T cells in control and SS2-infected mice at different stages. Scale bar = 50 μ m. **B** t-SNE maps showing the expression of specific marker molecules in T cells. **C** The t-SNE map shows the cluster partitions. **D** Phenotypic heatmap shows the phenotypic characteristics of the 13 clusters. **E** The

cluster frequency heatmap shows their distribution and the Spearman clustering according to the cell proportion in each sample. **F**, **G** t-SNE maps showing the expression of specific marker molecules in T cells and the proportion of specific subgroups in T cells. *N* = 4. Error bars represent the median \pm SEM. A one-way ANOVA or Dunnett's test was performed for analysis of multiple groups. *P* value < 0.05 (*); *p* < 0.01 (**); *p* < 0.001 (***) ; NS no significant difference.

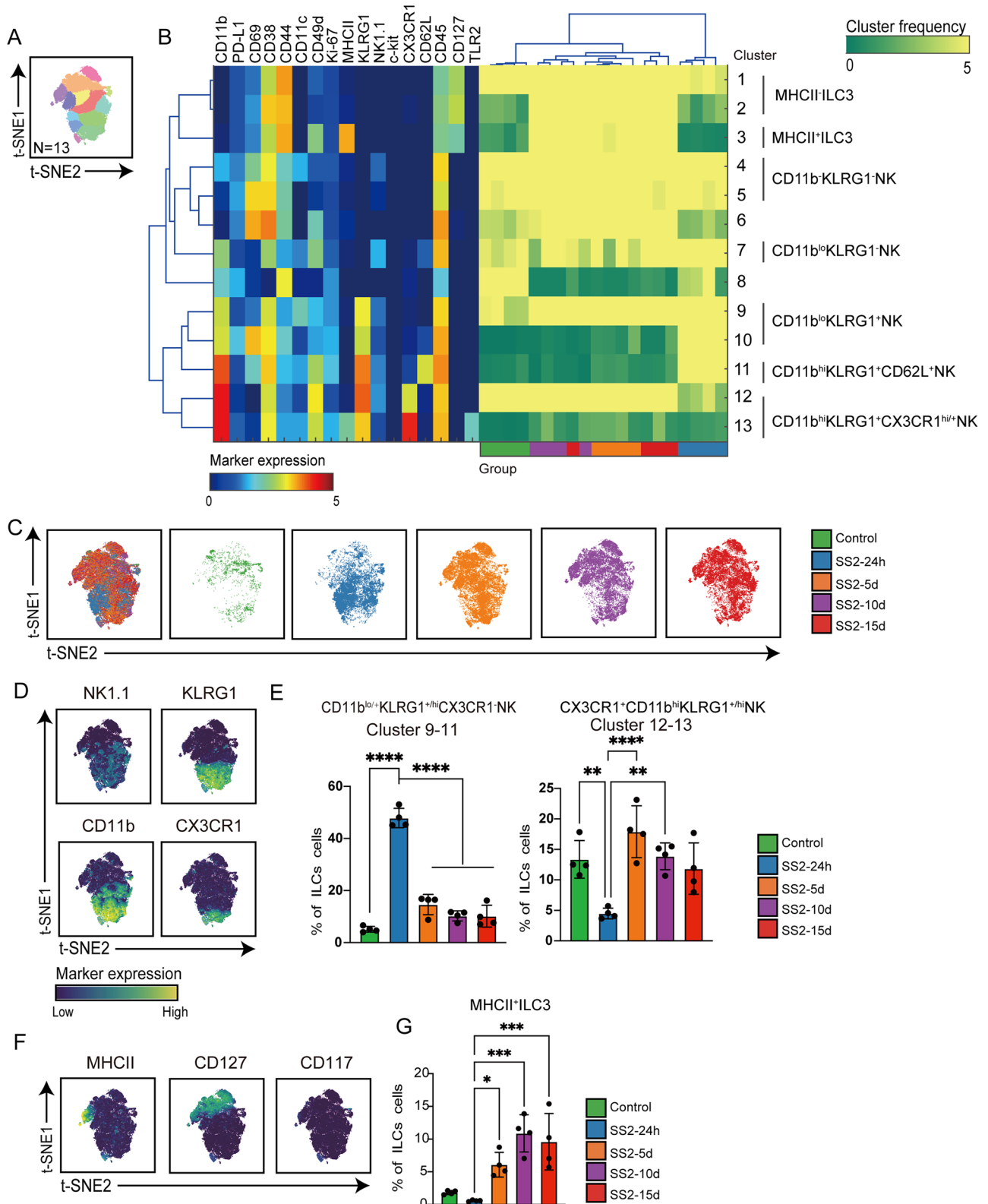


Fig. 6 | ILC in mouse brain exhibits NK and ILC3 subpopulations associated with meningitis. A The t-SNE map shows the cluster partitions. **B** Phenotypic heatmap shows the phenotypic characteristics of the 13 clusters. The cluster frequency heatmap shows their distribution and the Spearman clustering according to the cell proportion in each sample. **C** t-SNE plots of ILCs from the brain samples of five

groups are shown. **D, F** t-SNE maps showing the expression of specific marker molecules in ILCs. **E, G** The proportion of specific subgroups in ILCs. $N = 4$. Error bars represent the median \pm SEM. A one-way ANOVA or Dunnett's test was performed for analysis of multiple groups. P value < 0.05 (*); $p < 0.01$ (**); $p < 0.001$ (***) ; NS no significant difference.

Table 1 | Top six ranked clusters contributing to the infection time-specific t-SNE sample signatures

Nr	Control	SS2-24h	SS2-5d	SS2-10d	SS2-15d
1	Mac-6	Neu-1	Mon-6	T-7	B-1
	CD38 ⁺ MHCII ^{hi} BAMs	CD14 ^{hi} TLR2 ⁺ Neu	CD14 ^{lo} Ly6C ⁺ Mon	CD8 ⁺ Tem	CCR6 ⁺ MHCII ^{hi} B
2	DCs-1	Mac-5	Mac-9	ILC-3	B-6
	TLR2 ^{hi} CD11b ⁺ DCs	CD14 ^{lo} MHCII ^{hi} Mφ	CD38 ^{lo} Mφ	MHCII ^{hi} ILC3	CD11b ^{hi} CX3CR1 ⁺ B
3	ILC-12	Mon-1	T-9	T-1	Mac-2
	CD11b ^{hi} KLRG1 ⁺ NK	CD14 ⁺ Ly6C ⁺ Mon	KLRG1 ⁺ CX3CR1 ⁺ CD8 ⁺ Tem	CD4 ⁺ Tem	Ly6C ⁺ CD14 ^{hi} Mφ
4	DCs-5	ILC-7	DCs-6	T-13	ILC-1
	PD-L1 ^{lo} CD11b ⁺ DC	CD11b ^{lo} KLRG1 ⁺ NK	CX3CR1 ⁺ CD11b ⁺ DCs	CD11b ^{hi} CD8 ⁺ T	MHCII ^{hi} ILC3
5	Microglia-3	Mon-3	T-8	DCs-11	B-3
	MHCII ⁺ Ki-67 ⁺ Microglia	CD14 ⁺ Ly6C ⁺ CX3CR1 ^{hi} Mon	CD11c ⁺ CD8 ⁺ Tem	CX3CR1 ⁺ CD11b ⁺ DCs	CD11b ^{lo} B
6	B-4	Neu-6	T-5	T-4	B-2
	CD19 ^{lo} B	CD14 ^{hi} CX3CR1 ⁺ Neu	CD8 ⁺ Tem	KLRG1 ⁺ CD4 ⁺ Tem	CD38 ^{hi} MHCII ^{hi} B

when comparing the control with the neurological symptom group. The dominance of T cells (particularly CD11b^{hi}TLR2⁺MHCII⁺CD4⁺ and CD11c⁺CD8⁺ subsets) and B cells (CCR6⁺MHCII^{hi}) during the meningitic phases highlights the role of adaptive immunity in response to infection. The cytolytic function of CD11c⁺CD8⁺ T cells (Perforin/Granzyme B) parallels their role in viral encephalitis but is novel in bacterial meningitis. Similarly, CCR6⁺ B cells, known for homing to inflamed tissues, may facilitate antibody-independent immune modulation. Studies have shown that CCL20 is the only known high affinity ligand that binds with CCR6 and drives the migration of CCR6⁺ cells in tissues⁴⁷. Destroying the CCR6-CCL20 interaction by using antibodies or antagonists can prevent the migration of immune cells expressing CCR6 in inflammatory sites and reduce disease severity⁴⁸. This may become a potential therapeutic target for SS2 induced meningitis.

As a resource, our study has comprehensively characterized comprehensive immune cells in the mice brain throughout the disease process including the development of neurological symptoms after SS2 infection. Our study has some limitations. For example, we have focused on disease-specific changes in immune cell composition and phenotype at the single-cell protein level during the disease process, but not comprehensively analyzed accompanying cytokine changes. In addition, we selected several clusters of interest to validate their function, such as PD-L1⁺ neutrophils, but not all identified cell clusters. In future research, we will conduct in-depth biological studies on other key subsets. The spatial location of cell subpopulations in the during different stages of meningitis is still unclear, which need to further investigated by using technique such as imaging mass cytometry. Nevertheless, we have identified new cellular subsets in response to bacterial meningitis, and these and our results will form the basis of future work aimed at novel therapeutic interventions to decrease the burden of SS-meningitis.

Methods

Bacterial strains, and conditions

S. suis strain JZLQ022 was isolated from the brain of a meningitic pig. Culture and viability were done as described previously in our laboratory⁴⁹. Briefly, a single colony was transferred into a 5 mL Brain Heart Infusion (BHI) containing 5% (v/v) fresh foetal bovine serum (FBS) and incubated at 37 °C for 10 hours (h). Bacteria were quantified by multiple dilutions and adjusted by optical density (OD) with a spectrophotometer. The absorbance was 1.0 ± 0.1 at OD_{630nm} to obtain 1 × 10⁸ CFU (colony forming units).

Experimental infection

Female, 4–6 week aged ICR (Institute of Cancer Research) female mice were purchased from Liaoning Changsheng Biotechnology Co., Ltd (Production License Number. SYXK2020-0001). Animals were maintained in a 12 h-light/12 h-dark cycle environment with free access to rodent chow and

water. All mice were randomly divided into 5 groups. Then, mice were intraperitoneally injected with 1.3–1.4 × 10⁸ CFU SS2: mice showed typical neurological symptoms 5 days (d) post-infection. We collected brain samples of mice 24 h after infection (SS2-24h) when neurological symptoms appeared (SS2-5d), neurological symptoms lasted for 5 days (SS2-10d), and neurological symptoms lasted for 10 days (SS2-15d). The control group mice were injected with an equal amount of physiological saline. Observe the clinical symptoms of infected mice daily, and consider weight loss of over 20% as a humane endpoint. All animal experiments were conducted in accordance with the guidelines established by the Institutional Animal Care and Committee of Jilin University and approved by the Institutional Animal Care and Committee of Jilin University (Approval number SY202201009). We have complied with all relevant ethical regulations for animal use.

Tissue harvesting and single-cell suspension preparation

Mice were sacrificed 0 h and 24 h post-infection, within 24 h of meningitis onset, lasting for 5 and 10 days, respectively. Mice were anesthetized by intraperitoneal injection of 1% pentobarbital sodium, followed by cardiac perfusion using cold PBS for 5 minutes (min) per mouse. We mixed six mouse brain tissues into one sample, with four samples in each group. After complete removal of brain tissue, the pia mater, their surrounding brain parenchyma and choroid plexus were processed into single cells. Briefly, the brain was cut into small pieces and incubated with digestion buffer (RPMI supplemented with 2 mg/mL Collagenase IV and 0.2 mg/ml DNaseI) for 30 min rotating at 500 RCF(g) at 37 °C. Enzymatic digestion was stopped with FBS, the sample was filtered through a 70 μm cell filter to obtain a single-cell suspension. This was followed by gradient centrifugation with 30% and 70% Percoll (GE Healthcare Life Sciences) in PBS (v/v) (500 g for 30 min at 18 °C)⁵⁰. Throughout the digestion procedure, samples were maintained on ice until addition of mass cytometry antibodies.

Mass cytometry

Approximately 3 × 10⁶ cells per sample and a guaranteed survival rate of over 90%. Antibodies used for mass cytometry are listed in Supplementary Table 1. Coupling antibodies with corresponding metal tags to prepare metal tag conjugated antibodies and diluting them to the optimal staining concentration²⁴. The cells were resuspended and stained with Live/Dead 194Pt Cisplatin (Fluidigm) for 5 min and incubated with Fc Receptors Blocker Mixture (Equitech-Bio; anti-human/mouse/hamster/rat IgG) to block the non-specific Fc binding. Next, the cells were co-incubated with surface staining antibodies for 30 min. Subsequently, the cells were incubated overnight with Fix and Perm buffer (Fluidigm) supplemented with 191Ir and 193Ir DNA markers (Fluidigm) at 4 °C. Samples were washed twice with cell staining buffer and incubated with intracellular staining

antibodies for 30 min. Finally, cells were acquired with a Helios mass cytometer (Fluidigm), and data were normalized using EQ Four Element Calibration Beads (Fluidigm)²⁴.

Data processing and analysis

FlowJo (version 10.4) was used to identify single, live, CD45^{lo/+} immune cells. Next, all immune cells were analyzed using Cytoplex^{+H-SNE} software²³. In Cytoplex^{+H-SNE}, we excluded CD45^{lo/+} Ly6C⁺ endothelial cell clusters and zoomed in the remaining immune cell clusters. To visualize high-dimensional data, the t-SNE dimensionality reduction algorithm was applied to all samples²³. The default setting (Perplexity: 30; Iteration: 1000) is used for hierarchical random neighbor embedding (H-SNE) analysis. All H-SNE, t-SNE plots, and Gaussian Mean shift clustering-derived cell clusters were generated by the Cytoplex software. Each cell cluster contained at least 100 cells. In Matlab 2016, hierarchical clustering of phenotypic heatmaps was performed using Euclidean correlation and average linkage clustering methods⁵¹. For the cluster t-SNE maps, the data matrix with cluster frequencies of CD45^{lo/+} cells in the individual samples was normalized and computed to select the top 10 highest variance principal components as input to the t-SNE analysis, where the clusters with similar profiles clustered together. Median expression was obtained by FlowJo (version 10.4) analysis.

Flow cytometry

The single-cell suspension of mouse brain immune cells was obtained according to the above method. Cells were diluted to $1 \times 10^6/100 \mu\text{L}$ and incubated with a non-specific binding-blocking reagent cocktail of anti-mouse CD16/CD32 antibody (93, BioLegend). For cell surface antigen staining, cells were stained with the following fluorochrome-conjugated antibodies, PerCP-Cy5.5-anti-mouse CD45, PE-Cy7-anti-mouse CD45 (30-F11, 1:80, BioLegend), BV421-anti-mouse CD11b (M1/70, 1:200, BioLegend), APC-Cy7-anti-mouse CX3CR1 (SA011F11, 1:150, BioLegend), BV605-anti-mouse MHCII (M5/114.15.2, 1:150, BioLegend), PE-anti-mouse PD-L1 (11F6, 1:180, BioLegend), PerCP-Cy5.5-anti-mouse Ly6G (1A8, 1:100, BioLegend), PerCP-Cy5.5-anti-mouse CD3 (17A2, 1:400, BioLegend), APC-Cy7-anti-mouse CD11c (N418, 1:20, BioLegend), APC-anti-mouse CD8 (53-6.7, 1:200, BioLegend). Cultured cells were washed twice using FACS buffer and stained with surface markers for 30 min at 4 °C. cells were filtered with a 70 μm cell strainer before data acquisition on a flow cytometer (Beckman, USA). For intracellular cytokine staining, brain single cells were stimulated with (Phorbol 12-myristate 13-acetate (PMA) (50 ng/mL, Sigma) and ionomycin (1 mg/mL, Sigma) for 2 h at 37 °C, and 1x brefeldin A and monensin solution (BioLegend) were added for the final 4 h. Cultured cells were washed twice using FACS buffer and stained with surface markers for 30 min at 4 °C. The cells were then fixed, permeabilized with Cyto-Fast™ Fix/Perm Buffer Set (BioLegend) for 20 min at room temperature and incubated with intracellular antibodies (APC-anti-mouse IL-6 (MP5-20F3, 1:20, BioLegend), APC-anti-mouse TNF- α (MP6-XT22, 1:20, BioLegend), PE-anti-mouse IFN- γ (XMG1.2, 1:20, BioLegend), PE-anti-mouse Perforin (S160069A, 1:20, BioLegend), FITC-anti-mouse Granzyme B (QA16A02, 1:20, BioLegend) for 30 min at 4 °C. After washing the cells with FACS buffer once, cells were analyzed on a flow cytometer (Beckman, USA), and data were analyzed with FlowJo (version 10.4). The gating strategy for all flow cytometry data was presented in the supplementary information.

Monocyte adoptive transfer

For adoptive cell transfer of monocytes, mice peripheral blood monocytes (CD11b⁺Ly6C⁺F4/80^{lo}) were stained and sorted on a FACS Aria III (BD Biosciences) to achieve a purity > 95%. Then labeled with CellTrace violet (Thermo Fisher) for 20 min. Cells were washed with PBS to remove unbound dyes. 5×10^6 cells were intravenously transferred into recipient mice infected with SS2 for 2 h. After 12 h, CellTrace violet-positive donor monocyte-derived cells recovered from recipient brains were analyzed by flow cytometry.

Immunohistochemistry and immunofluorescence

Mice were deeply anesthetized by intraperitoneal injection of 1% pentobarbital sodium and transcardially perfused with 4% paraformaldehyde (PFA, Sigma-Aldrich) in PBS solution. The central nervous system (excluding the dura mater) was further fixed at 4 °C for 6–12 h, rinsed in PBS, and then cryoprotected in 30% (wt/vol) sucrose dissolved in PBS. Samples were embedded in OCT compound (Sigma-Aldrich). Cryosections with a thickness of 12–30 μm were prepared using a Hyrax C60 cryostat (Zeiss)⁶. Sections were pretreated with heat-mediated antigen retrieval for 15–20 min in sodium citrate buffer (0.1 mM) (pH 6.0) and sections were incubated overnight at 4 °C in diluted IBA-1 antibody (Abcam ab108539 1:500), Ly6G antibody (Abcam ab25377 1:500), CD3 (Abcam ab16669 1:500), Mac 2 (Abcam ab76245 1:1000), CD19 (Abcam ab245235 1:500) and CD206 (Abcam ab64693 1:500), respectively. Immunohistochemical staining was performed using the IHC (MXb, CN) and DAB (MXb, CN) kits according to the manufacturer's instructions. Next, sections were washed with distilled and then with tap water, counterstained with hematoxylin for 5 min, washed with tap water, dehydrated with ethanol, treated with xylene, and then mounted with neutral resin. For immunofluorescence staining, the sections are blocked with 10% goat serum (Sigma). Subsequently the sections were stained with primary antibodies (IBA-1, CD206, Ly6G, Ly6C, CD3, CD19, CD38, CD11c (Servicebio, 1:500)) in 1% PBS-T (overnight, 4 °C). And then stained with secondary antibodies in 1% PBS-T (1.5 h, room temperature). The sections were stained with DAPI (Sigma) solution for 5 min and washed twice with PBS. Finally, all slides were observed and scanned with a PANNORAMIC MIDI II automatic digital slide scanner (3DHISTECH, Budapest, Hungary). The statistical results were completed by ImageJ (version:2.3.0) software.

Laser confocal imaging

PD-L1⁺ and PD-L1⁻ neutrophils were placed on the climbing piece after poly-L-lysine treatment. Then 4% paraformaldehyde (PFA) was used to fix the cells, and 0.5% Triton X-100 was used to penetrate the cells for 15 min after three PBS rinses to remove the PFA. Before immunostaining, 5% goat serum was used for blocking. Blocking solution was then replaced with staining solution (PBS with 0.1% Bovine Serum Albumin) containing the primary antibodies H3 (1:200, ImmunoWay) and MPO (1:200, Proteintech) at 4 °C overnight. Samples were washed at least 5 times with PBS-0.5% Tween (PBST) and then incubated with staining solution containing the secondary antibodies anti-mouse IgG conjugated with Alexa Fluor 488 (1:2000, Cell Signaling Technology) and anti-rabbit IgG conjugated with Alexa Fluor 594 (1:2000, Cell Signaling Technology) at room temperature for 1 h. The samples were washed five times with PBST, the blocking agent containing DAPI (4',6-diamidino-2-phenylindole) was added dropwise, and the coverslips were finally covered. Fluorescence imaging was performed using a laser confocal microscopy (AXR, Nikon).

Statistical analysis and reproducibility

The sample size (N, representing biological replicates per group) is provided in all figure legends. For key experiments, independent replication was performed a minimum of three times. Statistics were performed on Graphpad Prism 9 (GraphPad Software, San Diego, CA). Statistical differences between groups were determined using a one-way analysis of variance (ANOVA) or Dunnett's multiple comparison test. Student's t-test was used to compare the two groups. The data are presented as the mean \pm standard error of three independent replicates' mean (SEM). Statistical significance: P value < 0.05 (*); p < 0.01 (**); p < 0.001 (***) ; NS no significant difference.

Reporting summary

Further information on research design is available in the Nature Portfolio Reporting Summary linked to this article.

Data availability

Mass cytometry data of CNS leukocytes from female ICR mice (<https://community.cytobank.org/cytobank/experiments/122065>) are available

online. Numerical source data for graphs and charts can be found in Supplementary Data 1. All other data are available from the corresponding author on reasonable request.

Received: 29 September 2024; Accepted: 19 August 2025;
Published online: 30 August 2025

References

- Charabati, M., Rabanel, J. M., Ramassamy, C. & Prat, A. Overcoming the brain barriers: from immune cells to nanoparticles. *Trends Pharm. Sci.* **41**, 42–54 (2020).
- De Vlaminck, K. et al. Differential plasticity and fate of brain-resident and recruited macrophages during the onset and resolution of neuroinflammation. *Immunity* **55**, 2085–2102 e2089 (2022).
- Tan, L. Y. et al. Emergence of the brain-border immune niches and their contribution to the development of neurodegenerative diseases. *Front Immunol.* **15**, 1380063 (2024).
- Butovsky, O. & Weiner, H. L. Microglial signatures and their role in health and disease. *Nat. Rev. Neurosci.* **19**, 622–635 (2018).
- Munro, D. A. D. et al. Microglia protect against age-associated brain pathologies. *Neuron* **112**, 2732–2748 e2738 (2024).
- Van Hove, H. et al. A single-cell atlas of mouse brain macrophages reveals unique transcriptional identities shaped by ontogeny and tissue environment. *Nat. Neurosci.* **22**, 1021–1035 (2019).
- Castellani, G., Croese, T., Peralta Ramos, J. M. & Schwartz, M. Transforming the understanding of brain immunity. *Science* **380**, eabo7649 (2023).
- Brioschi, S. et al. Heterogeneity of meningeal B cells reveals a lymphopoietic niche at the CNS borders. *Science* **373**, <https://doi.org/10.1126/science.abf9277> (2021).
- Fittipaldi, N., Segura, M., Grenier, D. & Gottschalk, M. Virulence factors involved in the pathogenesis of the infection caused by the swine pathogen and zoonotic agent *Streptococcus suis*. *Future Microbiol.* **7**, 259–279 (2012).
- Fulde, M. & Valentin-Weigand, P. Epidemiology and pathogenicity of zoonotic streptococci. *Curr. Top. Microbiol. Immunol.* **368**, 49–81 (2013).
- Doran, K. S. et al. Host-pathogen interactions in bacterial meningitis. *Acta Neuropathol.* **131**, 185–209 (2016).
- Fu, Y. et al. Exploring the destructive synergy between IL-33 and Suiysin hemolysis on blood-brain barrier stability. *Microbiol. Spectr.* **12**, e0061224 (2024).
- Wang, J. et al. Interaction of fibrinogen and muramidase-released protein promotes the development of *Streptococcus suis* meningitis. *Front Microbiol.* **6**, 1001 (2015).
- Takeuchi, D. et al. The contribution of suiysin to the pathogenesis of *Streptococcus suis* meningitis. *J. Infect. Dis.* **209**, 1509–1519 (2014).
- Pinho-Ribeiro, F. A. et al. Bacteria hijack a meningeal neuroimmune axis to facilitate brain invasion. *Nature* **615**, 472–481 (2023).
- Dominguez-Punaro, M. C. et al. *Streptococcus suis* serotype 2, an important swine and human pathogen, induces strong systemic and cerebral inflammatory responses in a mouse model of infection. *J. Immunol.* **179**, 1842–1854 (2007).
- Segura, M. et al. Proinflammatory cytokine and chemokine modulation by *Streptococcus suis* in a whole-blood culture system. *FEMS Immunol. Med. Microbiol.* **47**, 92–106 (2006).
- Dominguez-Punaro Mde, L. et al. In vitro characterization of the microglial inflammatory response to *Streptococcus suis*, an important emerging zoonotic agent of meningitis. *Infect. Immun.* **78**, 5074–5085 (2010).
- Sofroniew, M. V. & Vinters, H. V. Astrocytes: biology and pathology. *Acta Neuropathol.* **119**, 7–35 (2010).
- Perry, V. H. & Teeling, J. Microglia and macrophages of the central nervous system: the contribution of microglia priming and systemic inflammation to chronic neurodegeneration. *Semin Immunopathol.* **35**, 601–612 (2013).
- Spitzer, M. H. & Nolan, G. P. Mass cytometry: single cells, many features. *Cell* **165**, 780–791 (2016).
- Jiang, X. et al. Brain immune cell infiltration and serum metabolomic characteristics reveal that lauric acid promotes immune cell infiltration in brain and *Streptococcus suis* meningitis in mice. *Mol. Neurobiol.* <https://doi.org/10.1007/s12035-024-04144-1> (2024).
- van Unen, V. et al. Visual analysis of mass cytometry data by hierarchical stochastic neighbour embedding reveals rare cell types. *Nat. Commun.* **8**, 1740 (2017).
- Li, N. et al. Mass cytometry reveals innate lymphoid cell differentiation pathways in the human fetal intestine. *J. Exp. Med.* **215**, 1383–1396 (2018).
- Lehnardt, S. Innate immunity and neuroinflammation in the CNS: the role of microglia in Toll-like receptor-mediated neuronal injury. *Glia* **58**, 253–263 (2010).
- Li, Q. et al. Developmental heterogeneity of microglia and brain myeloid cells revealed by deep single-cell RNA sequencing. *Neuron* **101**, 207–223 e210 (2019).
- Depp, C., Doman, J. L., Hingerl, M., Xia, J. & Stevens, B. Microglia transcriptional states and their functional significance: context drives diversity. *Immunity* **58**, 1052–1067 (2025).
- Van Hove, H., De Feo, D., Greter, M. & Becher, B. Central nervous system macrophages in health and disease. *Annu Rev. Immunol.* **43**, 589–613 (2025).
- Victor, M. B. et al. Lipid accumulation induced by APOE4 impairs microglial surveillance of neuronal-network activity. *Cell Stem Cell* **29**, 1197–1212 e1198 (2022).
- Guan, Z. et al. Injured sensory neuron-derived CSF1 induces microglial proliferation and DAP12-dependent pain. *Nat. Neurosci.* **19**, 94–101 (2016).
- Li, T. & Zhang, S. Microgliosis in the injured brain: infiltrating cells and reactive microglia both play a role. *Neuroscientist* **22**, 165–170 (2016).
- Rua, R. et al. Infection drives meningeal engraftment by inflammatory monocytes that impairs CNS immunity. *Nat. Immunol.* **20**, 407–419 (2019).
- Rebejac, J. et al. Meningeal macrophages protect against viral neuroinfection. *Immunity* **55**, 2103–2117 e2110 (2022).
- Mrdjen, D. et al. High-dimensional single-cell mapping of central nervous system immune cells reveals distinct myeloid subsets in health, aging, and disease. *Immunity* **48**, 380–395 e386 (2018).
- Mook-Kanamori, B. B., Geldhoff, M., van der Poll, T. & van de Beek, D. Pathogenesis and pathophysiology of pneumococcal meningitis. *Clin. Microbiol. Rev.* **24**, 557–591 (2011).
- Wang, J. F. et al. Up-regulation of programmed cell death 1 ligand 1 on neutrophils may be involved in sepsis-induced immunosuppression. *Anesthesiology* **122**, 852–863 (2015).
- Mangalam, A., Rodriguez, M. & David, C. Role of MHC class II expressing CD4+ T cells in proteolipid protein(91-110)-induced EAE in HLA-DR3 transgenic mice. *Eur. J. Immunol.* **36**, 3356–3370 (2006).
- Si, Y., Zhang, Y., Zuloaga, K. & Yang, Q. The role of innate lymphocytes in regulating brain and cognitive function. *Neurobiol. Dis.* **179**, 106061 (2023).
- Wang, J. F. et al. Upregulated PD-L1 delays human neutrophil apoptosis and promotes lung injury in an experimental mouse model of sepsis. *Blood* **138**, 806–810 (2021).
- Olivera, G. C., Ross, E. C., Peuckert, C. & Barragan, A. Blood-brain barrier-restricted translocation of *Toxoplasma gondii* from cortical capillaries. *Elife* **10**, <https://doi.org/10.7554/eLife.69182> (2021).
- Mrdjen, D., Hartmann, F. J. & Becher, B. High dimensional cytometry of central nervous system leukocytes during neuroinflammation. *Methods Mol. Biol.* **1559**, 321–332 (2017).

42. Hammond, T. R. et al. Single-cell RNA sequencing of microglia throughout the mouse lifespan and in the injured brain reveals complex cell-state changes. *Immunity* **50**, 253–271 e256 (2019).
43. Burgess, M., Wicks, K., Gardasevic, M. & Mace, K. A. Cx3CR1 expression identifies distinct macrophage populations that contribute differentially to inflammation and repair. *Immunohorizons* **3**, 262–273 (2019).
44. van de Laar, L. et al. Yolk sac macrophages, fetal liver, and adult monocytes can colonize an empty niche and develop into functional tissue-resident macrophages. *Immunity* **44**, 755–768 (2016).
45. Chen, H. R. et al. Monocytes promote acute neuroinflammation and become pathological microglia in neonatal hypoxic-ischemic brain injury. *Theranostics* **12**, 512–529 (2022).
46. Wang, J., Rattner, A. & Nathans, J. Bacterial meningitis in the early postnatal mouse studied at single-cell resolution. *Elife* **12**, <https://doi.org/10.7554/eLife.86130> (2023).
47. Meitei, H. T., Jadhav, N. & Lal, G. CCR6–CCL20 axis as a therapeutic target for autoimmune diseases. *Autoimmun. Rev.* **20**, 102846 (2021).
48. Hirota, K. et al. Preferential recruitment of CCR6-expressing Th17 cells to inflamed joints via CCL20 in rheumatoid arthritis and its animal model. *J. Exp. Med.* **204**, 2803–2812 (2007).
49. Sun, Q. et al. Ribosomal Protein SA-Positive Neutrophil Elicits Stronger Phagocytosis and Neutrophil Extracellular Trap Formation and Subdues Pro-Inflammatory Cytokine Secretion Against *Streptococcus suis* Serotype 2 Infection. *Front Immunol.* **11**, 585399 (2020).
50. Korin, B., Dubovik, T. & Rolls, A. Mass cytometry analysis of immune cells in the brain. *Nat. Protoc.* **13**, 377–391 (2018).
51. Li, N. et al. Memory CD4(+) T cells are generated in the human fetal intestine. *Nat. Immunol.* **20**, 301–312 (2019).

Acknowledgements

This study was supported by the National Key Research and Development Program of China (2021FYD1800405) and the National Natural Science Foundation of China (No.32072823). We thank Dr. Paul R Langford (Imperial College London) for helping us revise the language and providing valuable comments on the manuscript. We thank Dr. Zhang Jing from the Pathology Laboratory of Jilin University for his guidance on pathological sections. The graphic abstract was drawn by FigDraw (ID: SSYTU73e0f). The elements in panel A of Fig. 1 include mice and syringes were from SCIDraw (<https://doi.org/10.5281/zenodo.3925901>), while other elements were provided by FigDraw (ID: ROYPP0e640).

Author contributions

X.J.: Conceptualization, Data curation, Formal analysis, Investigation, Writing—original draft. J.M.: Formal analysis, Investigation, Writing—original draft. J.Z.: Formal analysis, Investigation, Writing—original draft. Y.T.: Formal

analysis, Investigation. T.W.: Data curation, Formal analysis. Z.L.: Investigation, Data curation. Z.W.: Investigation, Data curation. T.A.: Data curation, Formal analysis. F.L.: Formal analysis, Investigation. N.L.: Conceptualization, Writing—review & editing. L.L.: Conceptualization, Investigation, Writing—review & editing.

Competing interests

The authors declare no competing interests.

Additional information

Supplementary information The online version contains supplementary material available at <https://doi.org/10.1038/s42003-025-08748-8>.

Correspondence and requests for materials should be addressed to Na Li or Liancheng Lei.

Peer review information *Communications Biology* thanks the anonymous reviewers for their contribution to the peer review of this work. Primary Handling Editors: Rosie Bunton-Stasyshyn & Laura Rodríguez Pérez. A peer review file is available.

Reprints and permissions information is available at <http://www.nature.com/reprints>

Publisher's note Springer Nature remains neutral with regard to jurisdictional claims in published maps and institutional affiliations.

Open Access This article is licensed under a Creative Commons Attribution-NonCommercial-NoDerivatives 4.0 International License, which permits any non-commercial use, sharing, distribution and reproduction in any medium or format, as long as you give appropriate credit to the original author(s) and the source, provide a link to the Creative Commons licence, and indicate if you modified the licensed material. You do not have permission under this licence to share adapted material derived from this article or parts of it. The images or other third party material in this article are included in the article's Creative Commons licence, unless indicated otherwise in a credit line to the material. If material is not included in the article's Creative Commons licence and your intended use is not permitted by statutory regulation or exceeds the permitted use, you will need to obtain permission directly from the copyright holder. To view a copy of this licence, visit <http://creativecommons.org/licenses/by-nc-nd/4.0/>.

© The Author(s) 2025

¹State Key Laboratory for Diagnosis and Treatment of Severe Zoonotic Infectious Diseases, Key Laboratory for Zoonosis Research of the Ministry of Education, Institute of Zoonosis, and College of Veterinary Medicine, Jilin University, Changchun, China. ²Leiden Computational Biology Center, Leiden University Medical Center, Leiden, the Netherlands. ³Department of Pattern Recognition and Bioinformatics Group, Delft University of Technology, Delft, the Netherlands. ⁴These authors contributed equally: Xuan Jiang, Jikun Mei. ✉ e-mail: vettina2013@126.com; liliancheng@163.com